Chemical Physics Letters 468 (2009) 1–8

Contents lists available at ScienceDirect

Chemical Physics Letters

journal homepage: www.elsevier.com/locate/cplett

FRONTIERS ARTICLE

Tomography of a supersonically cooled molecular jet using cavity-enhanced direct frequency comb spectroscopy

Michael J. Thorpe *, Florian Adler, Kevin C. Cossel, Marcio H.G. de Miranda, Jun Ye

JILA, National Institute of Standards and Technology and University of Colorado, Department of Physics, University of Colorado, Boulder, CO 80309-0440, USA

ARTICLE INFO

Article history:
Received 9 November 2008
In final form 19 November 2008
Available online 27 November 2008

ABSTRACT

Cavity-enhanced direct frequency comb spectroscopy is used to obtain simultaneously high resolution and broad spectral-bandwidth measurements of a supersonically cooled jet of acetylene molecules. We demonstrate a complete spatial mapping of density, velocity, and internal state distributions of a cold molecular jet via tomographic reconstructions. These measurements reveal interesting and never-before-observed features of the pulsed jet expansion, including anomalous C_2H_2 absorption lineshapes and anomalous spatial variations of the rotational temperature distribution. The demonstrated capabilities establish this technique as a powerful new tool for studies of cold molecules.

1. Introduction

Cavity-enhanced direct frequency comb spectroscopy (CE-DFCS) is a spectroscopic technique that combines the broad spectrum of an optical frequency comb with the high sensitivity to optical loss provided by a femtosecond enhancement cavity [1–4]. The individual 'teeth' of the frequency comb [5,6] are resonantly coupled into the modes of the enhancement cavity where molecular detection takes place. The high sensitivity of the optical cavity modes to intra-cavity loss enhances the molecular absorption signal by several orders of magnitude [7–12]. Light transmitted from the cavity preserves the original frequency structure of the comb, but also carries the additional information of the intra-cavity absorption pattern. The absorption pattern is recovered by frequency resolving the transmitted beam and simultaneously recording the absorption experienced by each comb tooth in a parallel fashion.

CE-DFCS allows the unique capability to observe molecular ensembles with simultaneous broad spectral coverage, high resolution, and high detection sensitivity [4,3]. These capabilities are attractive for a variety of experimental situations. For example, CE-DFCS has already proven extremely useful for investigating complex mixtures of molecular species at low concentrations due to its high sensitivity and broad spectral coverage [13]. Additionally, ensembles involving complex velocity and internal state dynamics are also ideal candidates for CE-DFCS studies because the high resolution capability allows the observation of correlations between the internal energy states and their external motions. For instance, CE-DFCS will be an ideal tool for the emerging field of cold molecule physics and cold chemistry, where experimental conditions involve small numbers of molecules, narrow resonances, and potentially many internal energy states for different species [14–19]. Indeed, femtosecond pulse trains and frequency combs are already being used for population transfer and coherent control of cold molecules [20–23].

As a first effort in making a complete characterization of cold molecular ensembles with CE-DFCS, we have performed a tomographic reconstruction of absorption measurements from a supersonically cooled jet of C_2H_2 molecules. Tomographic reconstructions are enabled by the use of a movable jet nozzle, allowing us to measure the integrated absorption through the supersonic jet at a variety of distances from the nozzle and heights from the jet axis. The precise frequency control of the comb allows us to record the absorption lineshapes at each measurement position, while the broad spectral coverage of the comb allows us to record the entire $\nu_1 + \nu_3$ rovibrational band of C_2H_2 (both P and R branches) in a single measurement. As a result, the transverse velocity distributions of the molecules in the jet and their corresponding internal energy states are determined at the same time. Due to these capabilities, the use of CE-DFCS provides unprecedented advantages over previous supersonic jet studies that used Raman spectroscopy or continuous-wave cavity ringdown spectroscopy for supersonic beam investigations [24–27]. The ability to simultaneously observe the internal and external energies of the molecular jet allows us to rapidly generate spatial maps of the density, velocity, and internal state distributions via tomographic reconstruction [28], essentially providing a thermodynamic snapshot of the entire jet.

The tomographic reconstructions presented in this Letter reveal several interesting features of the pulsed supersonic jet. First, we find spatially varying anomalous lineshapes that, to our knowledge, have not been previously reported. We also observe an anomalous rotational temperature map that suggests that the coldest temperatures in the jet are not at the center, but rather

* Corresponding author.
E-mail address: thorpe@jilaul.colorado.edu (M.J. Thorpe).

0009-2614/$ - see front matter © 2008 Elsevier B.V. All rights reserved.
doi:10.1016/j.cplett.2008.11.064

form a ring around the axis of the jet. We also infer that the radial velocity is strongly correlated with the radial positions of the molecules in the beam. Finally, we present evidence indicating a transverse velocity dependence of the rotational cooling rate of the molecules within the expansion.

2. Experiment

A CE-DFCS system consists of three basic building blocks shown in Fig. 1: a mode-locked laser, a high finesse detection cavity, and a frequency resolving spectrometer in cavity transmission. The mode-locked laser emits a train of femtosecond pulses. In the frequency domain, the laser output generates a broad frequency spectrum. As an example of the spectral coverage that can be achieved with mode-locked sources, an Er^{+3} fiber laser can generate a spectrum covering 1.0–2.3 μm when spectral broadening via highly nonlinear fiber is implemented [29]. Under this broad spectral envelope are a comb of narrow and evenly spaced frequency modes, wherein the nth mode has the frequency $\nu_n = nf_r + f_o$ [5,30]. The spacing between the comb modes is the repetition frequency (f_r), which is the inverse of the time between the pulses emitted from the laser. The erbium fiber laser used in the present work has an f_r of 100 MHz. f_r is controlled by changing the laser cavity length, in this case via a fast (20 kHz bandwidth) short-travel (2 μm) fiber stretcher and a slow (100 Hz bandwidth) long-travel (13 μm) piezo electric transducer (PZT). The second frequency that determines ν_n is the carrier-envelope-offset frequency (f_o), which arises from the difference between the group velocity and phase velocity of pulses in the laser cavity [31]. f_o can have values in the range $-\frac{f_r}{2} \leqslant f_o \leqslant \frac{f_r}{2}$ and acts to shift the entire comb in frequency space. f_o can be controlled by adjusting either the laser pump power or a dispersive element (e.g. a wave plate) inside the laser cavity. After one amplification stage, the average power of our erbium fiber laser is 130 mW in the spectral range between 1.5 μm and 1.6 μm. Accordingly, each comb mode has ~1 μW of power available for performing spectroscopic measurements.

The train of femtosecond pulses is resonantly coupled into a high finesse optical cavity where the molecular detection takes place [32]. There are several strategies to achieve efficient coupling [33,3,4]. In the present work, a cavity free spectral range (FSR) of 700 MHz is chosen to be seven times that of f_r (100 MHz) such that every seventh comb mode is coupled to the cavity. This choice of FSR acts to filter the comb modes as shown in Fig. 1 so that each molecular absorption line, having a nominal Doppler linewidth of 350 MHz, only interacts with one comb mode. The comb teeth are rapidly swept over the cavity modes by modulating the laser f_r, and absorption measurements are performed using the technique of transient cavity-enhanced absorption spectroscopy [4,34]. The cavity is constructed from two 2-m radius of curvature mirrors with a reflectivity of 99.95%, resulting in a finesse of 6300. The TEM_{00} cavity mode has a 1/e electric field diameter of 1 mm which sets the spatial resolution limit of the tomographic measurements presented in this Letter. The Rayleigh range of the cavity mode is 50 cm such that its diameter is nearly constant over the length of the cavity. To avoid degrading the finesse by scattering loss from the supersonic expansion nozzle, the cavity mode must be positioned at least 2.5 mm from the nozzle. This requirement sets the minimum distance from the nozzle that measurements can be made with the current system. Of course, engineering a smaller diameter cavity mode would allow for both higher spatial resolution and measurements closer to the expansion nozzle. One of the cavity mirrors is mounted on a 1 in diameter ring PZT for servoing of the cavity length at bandwidths of up to 1 kHz. Large changes to the cavity length are made by a resistive heater that holds the cavity structure at a nominal temperature of 35 °C.

A virtually-imaged phased-array (VIPA) spectrometer is used to resolve and simultaneously record the spectrum transmitted from the cavity within a 25 nm spectral range from 1.515 μm to 1.54 μm [35]. The light transmitted from the cavity is focused via a cylindrical lens into the VIPA etalon, which disperses the light in the vertical direction. The etalon is slightly tilted in the vertical direction such that the focused beam is incident at an angle of 2°. The light transmitted from the VIPA etalon is then dispersed in the horizon-

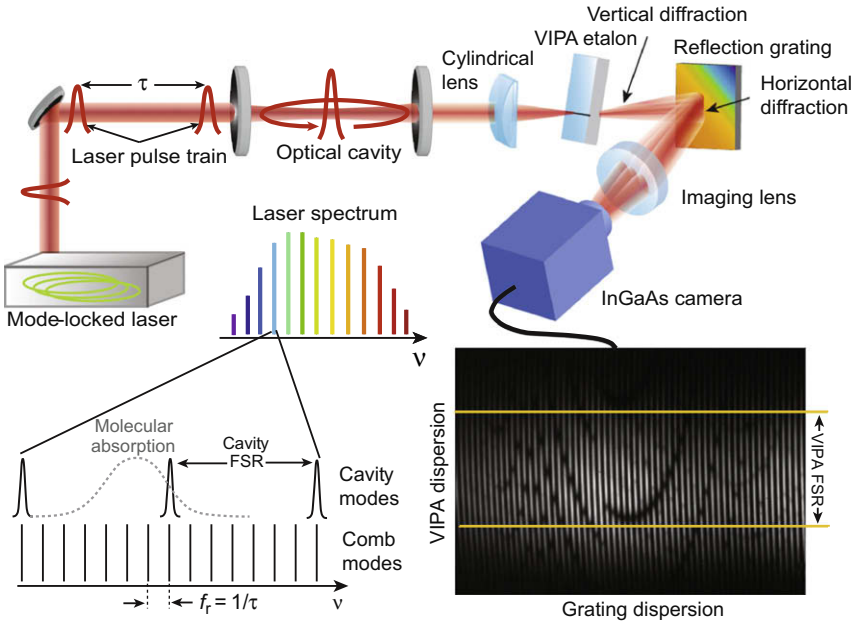

Fig. 1. (a) Schematic of the basic CE-DFCS system. A mode-locked laser generates a pulse train that is coupled into a high finesse detection cavity. The light transmitted from the cavity is analyzed using a VIPA spectrometer producing an interference image (bottom right). The parabolic patterns of dark spots are due to CO_2 absorption at 1.6 μm. The frequency diagram (bottom left) shows how the comb modes are coupled into the high finesse cavity. The molecular absorption line is measured by scanning both the comb and cavity modes over 1 FSR of the cavity.

tal dimension by a diffraction grating and imaged by a lens onto the focal plane of a 320 × 256 pixel InGaAs camera. When imaged, light transmitted from the VIPA spectrometer produces a two-dimensional (2D) interference pattern that is a combination of the horizontal grating dispersion and the vertical VIPA etalon dispersion (Fig. 1). The large VIPA dispersion provides high resolution in the vertical direction while the lower grating dispersion acts to resolve the mode orders of the VIPA transmission. To retrieve a resolved interference pattern at the focal plane, the grating resolution must be higher than the FSR of the VIPA etalon. The etalon used in this experiment has an FSR of approximately 50 GHz. A grating with 1100 lines/mm is used with a 20 cm focal length imaging lens to achieve a resolution of 25 GHz in the horizontal direction. As a result, the interference image in Fig. 1 shows dark stripes separating the bright vertical fringes, indicating that the mode orders of the VIPA etalon are well-resolved.

The precise values of both the spectrometer resolution and the VIPA FSR depend on the angle of incidence of the cavity transmitted beam on the etalon. Furthermore, the spectrometer resolution also depends slightly on the vertical position of the observed absorption feature within the interference pattern. These effects have been studied in depth by Weiner et al. who developed a generalized grating equation for the VIPA etalon and beam propagation equations for mapping transmitted wavelengths to their positions in the interference image [36–38]. Accordingly, we performed careful measurements of the VIPA FSR and position-dependent resolution of the spectrometer prior to the C_2H_2 jet experiment. These measurements were performed by observing the cavity transmitted absorption spectrum of a dilute sample of C_2H_2. Using the well-known transition frequencies of the $\nu_1 + \nu_3$ rovibrational band of C_2H_2, the VIPA FSR was determined to be 49.52 GHz [39,40]. The spatially varying spectrometer resolution was determined by comparing the spatial extent of absorption transitions that appeared at different heights on the interference image to the VIPA FSR interval. The VIPA spectrometer configuration used in the present work has a resolution that varies from 1.0 GHz at the bottom of the FSR interval to 1.3 GHz at the top of the interval. Due to the 700 MHz spacing of the cavity transmitted comb modes and the Lorentzian transfer-function of the VIPA etalon transmission, each resolvable frequency channel recorded by the InGaAs camera samples an average of 2.5 comb modes. This acts to dilute the signal carried by each comb mode that interacts with the intra-cavity absorption. However, since only one comb mode is interacting with the molecular absorption within each resolvable channel, the frequency resolution of the measurement is not limited by the VIPA spectrometer, but rather by the stability of individual comb modes.

To demonstrate high resolution and stable frequency measurements, the cavity mode frequencies are stabilized to within 700 kHz using a frequency stabilized Nd:YAG laser [41]. The comb frequencies are slaved to the cavity modes using a servo scheme described in Ref. [4]. Frequency scans of the comb and cavity modes are performed by stepping the frequency of the 1.064 μm Nd:YAG laser in 25 MHz steps over 1 GHz, resulting in a 700 MHz (1 FSR) total scan of the cavity mode frequency at 1.525 μm made in 17.5 MHz steps. The 650 m/s average forward velocity of molecules moving through the 1 mm diameter cavity mode results in a transit-time broadened linewidth of 200 kHz. Accordingly, resolutions of better than 1 MHz can be achieved, which is more than sufficient to record the nominal Doppler-limited linewidth for molecules in the jet. Meanwhile, the VIPA spectrometer records 25 nm spectral snapshots, easily capturing the entire cooled rotational spectrum of the C_2H_2 molecules in a single measurement.

To create the pulsed supersonic expansion, a mixture of 2.5% C_2H_2 and 97.5% Ar at 650 Torr is allowed to expand through a 1 mm diameter circular valve into an evacuated chamber with pressure $<10^{-5}$ Torr. The nozzle was constructed with a pseudo-trumpet geometry shown in Fig. 5 as a compromise between ease of manufacturing and optimal cooling and forward collimation of the molecular beam [42]. The pulsed valve is operated at a rate of 2 Hz and is held open for 650 μs, creating molecular packets of the same duration. The expanding jet of molecules is oriented perpendicularly to the mode of an optical cavity where CE-DFCS measurements are performed. The valve is mounted in a bellows and on translation stages, allowing control of the distance from the valve to the cavity mode (z-coordinate) and the height of the valve with respect to the cavity mode (y-coordinate) (Fig. 2a). Specifically, the z-coordinate is measured from the tip of the expansion nozzle (Fig. 5), and the y-coordinate is measured from the jet axis. Due to the mobility of the valve, line integrals along the cavity mode (x-coordinate) of the absorption through the beam can be performed at a variety of positions, allowing for tomographic reconstruction. The tomographic reconstructions are used to determine the exact position of the jet axis ($y = 0$).

To characterize the time-dependent shape and forward velocity of our molecular packet, we measured the pulse shape for $y = 0$ mm at four different distances from the nozzle ($z = 3.5$, 8.5, 13.5 and 18.5 mm). At each z-position we varied the time delay between opening the valve and performing the absorption measurement to map out both the pulse shape and the arrival time of the front edge of the pulse. From these measurements, we determined that the average forward velocity of our jet was 650 ± 25 m/s. The molecular pulse shape resembled a plateau with sharp front and back edges and a flat top at all measurement positions. The repeatability of these measurements indicated that our control of the valve opening time was better than ±5 μs.

Fig. 2b shows the cooled C_2H_2 rotational spectrum at a distance of $z = 6$ mm from the nozzle. This spectrum is an average of 10 measurements for a total acquisition time of 5 s. Frequency scans of the cavity over one FSR are made by successively changing the cavity length to map out the entire frequency spectrum within the 25 nm bandwidth of the VIPA spectrometer. Fig. 2c shows a one FSR frequency scan of the peak absorption wavelengths of the 0 through 5 transitions of the R-branch. This scan was performed in approximately 30 min, and yielded lineshape measurements for each of the P and R branch transitions. For the frequency scans in Fig. 2c, the valve height was $y = 1$ mm such that the cavity mode was approximately 1 mm below the axis of the molecular beam. The minimum detectable integrated absorption of the system is 1×10^{-6} at 1 ms of integration time. For the typical temperature and diameter of our beam ($T = 10$ K and $d = 1$ cm), the minimum detectable concentration of C_2H_2 is 1.7×10^{11} cm^{-3}.

3. Discussion

So far, we have presented an overview of our measurement system and discussed how we take integrated absorption measurements at many positions through the supersonic jet. While the integrated absorption measurements provide us with general information about the size, density and temperature of the supersonic jet, tomographic reconstructions are required to obtain the exact values of each quantity for specific positions within the jet. In the first half of this section we will describe how we implement tomography to convert the integrated absorption measurements into maps of the density and temperature of the supersonic jet. The second half of the discussion will be devoted to an analysis of the tomographic reconstruction that reveals interesting properties of the jet.

In the present work, our measurements are restricted to parallel integrated absorption measurements as a function of height from

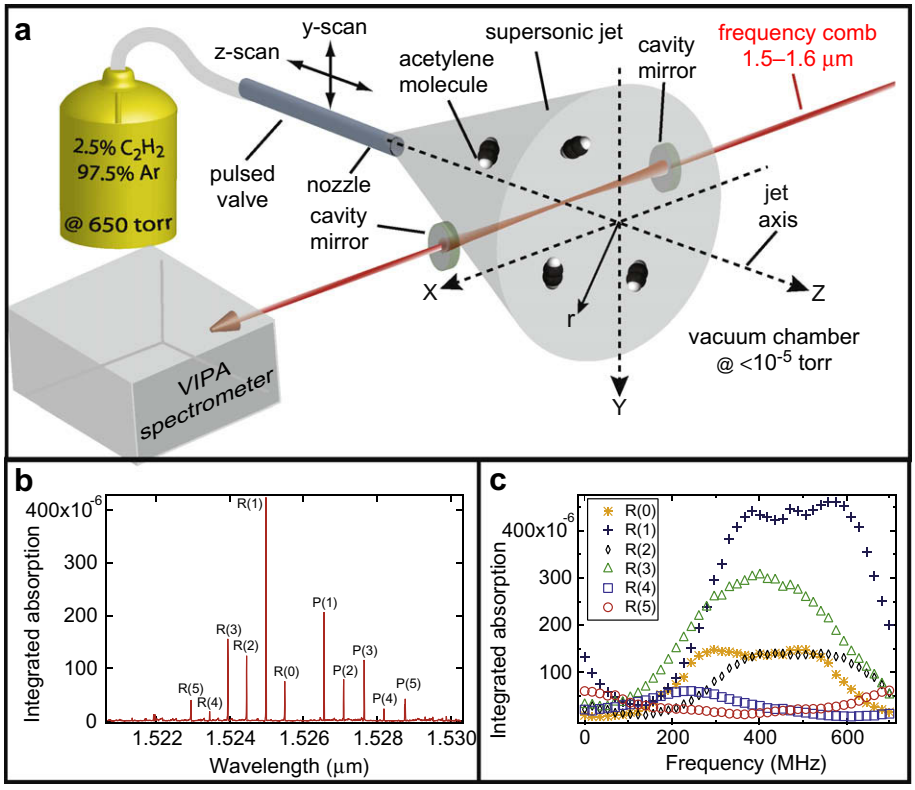

Fig. 2. (a) Schematic of the supersonic jet measurement via CE-DFCS. (b) A snapshot of the rotational spectrum of the C_2H_2 beam at $z = 6$ mm, $y = 1$ mm. (c) The peak absorption values for the R-branch transitions at $z = 6$ mm and $y = 1$ mm as the cavity length is scanned through one FSR in 17.5 MHz steps. The rotational spectrum snapshot in (b) was captured at a frequency of 600 MHz during the scan in (c).

the jet axis. Since our scheme provides measurements at only one angle through the supersonic jet, our tomographic reconstructions are limited to distributions that are axis-symmetric [28]. In this case, an inverse Abel transform is used to convert the single set of parallel integrated absorption measurements into a radial absorption distribution $\alpha(r)$, where r is the radial position [28]. We justify our assumption of a radially symmetric jet based on our use of the cylindrically symmetric nozzle shown in Fig. 5. Furthermore, we have performed frequency scans of the integrated absorption both above and below the jet axis which yield very similar absorption lines, both in shape and intensity. Evidence of the agreement between above and below axis measurements can be seen by comparing the $y = -1.1$ mm and $y = 0.9$ mm measurements in Fig. 3a. For jets that lack axial symmetry, our general approach can still be implemented; however, the number and type of measurements required to reconstruct the beam are significantly more extensive. In the asymmetric case, sets of parallel height-dependent measurements must be performed at a variety of angles covering 180° through the jet, and the more complicated Radon transform must be implemented to reconstruct the asymmetric absorption distribution $\alpha(r,\phi)$ [43].

The steps for performing tomographic reconstructions of the radial absorption distribution are shown in Fig. 3 using data from the P(2) transition at a nozzle distance of $z = 11$ mm. First, each of the integrated absorption lineshapes is fit to a sum of three Gaussians (Fig. 3a). This fitting function was chosen because it provided an excellent fit to every absorption lineshape that we observed. The triple Gaussian lineshape implies that the distribution of rotational ground states are populated differently in the center of the beam than in surrounding region. This is a point that will be discussed in more detail in conjunction with Fig. 6. Next, the fitted curves at each height were integrated along the frequency axis yielding

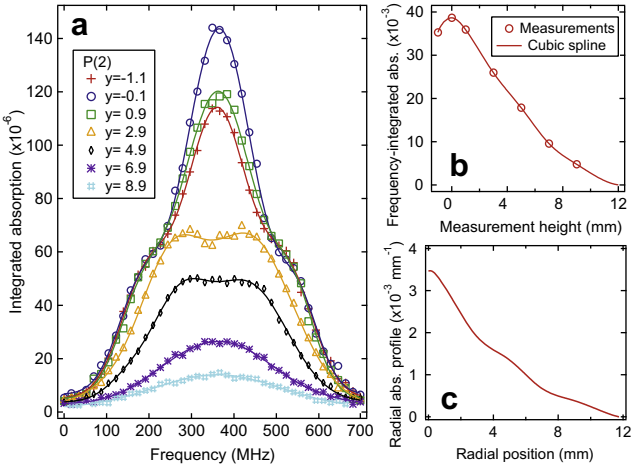

Fig. 3. (a) Integrated absorption frequency scans (integrated along x-axis) of the P(2) transition at a distance of $z = 11$ mm from the nozzle for several heights of the cavity mode with respect to the axis of the expansion. (b) The data from (a) are frequency-integrated and plotted versus the measurement height. A cubic spline of this data is performed in preparation for the inverse Abel transform. (c) The inverse Abel transform of the cubic spline curve in (b) results in a radial absorption profile.

net absorption versus height (Fig. 3b). The data points in Fig. 3b were interpolated using a cubic spline. Finally, the spline of the integrated absorption data was converted to a radial absorption distribution using the inverse Abel transform:

$$\alpha(r) = -\frac{1}{\pi}\int_r^\infty \frac{d\alpha(y)}{dy}\frac{dy}{\sqrt{y^2 - r^2}}. \quad (1)$$

Here, $\alpha(y)$ represents height-dependent integrated absorption measurements (integrated along x) and $\alpha(r)$ is the radial absorption distribution. Since this integral has a singularity at $y = r$, direct integration of this transform results in inaccurate reconstructions of radial distribution. Consequently, there is an extensive literature concerning various algorithms that can be used to overcome the singularity issue. We have selected a discrete inverse Abel transform algorithm based on an eigenvalue approach to provide rapid and accurate tomographic reconstructions of the radial absorption profile [44].

Using the above procedure, the radial absorption distributions were calculated for each R-branch rotational transition at the nozzle distance $z = 11$ mm as shown in Fig. 4a. The rotational absorption distribution at each radial position can be used to determine the molecular rotational temperature and density distributions via the relation $\alpha(v) = \rho S_i g(v)$. Here $\alpha(v)$ is the absorption per unit length, $g(v)$ is the absorption lineshape, S_i is the line intensity, and ρ is the density. When the molecular ensemble is in thermal equilibrium, the line intensities of the rotational transitions can be described by a Boltzmann distribution [45,46]

$$S_i = g_I L_i v C s_i, \quad \text{where } s_i = \frac{e^{-\frac{E_j}{k_B T_R}}}{Q_r}. \tag{2}$$

Here, j is the ground state rotational quantum number, E_j is the ground state energy of the jth rotational level, g_I is the nuclear spin state degeneracy (3 for odd and 1 for even rotational ground states), k_B is the Boltzmann constant, and T_R is the rotational temperature of the molecular ensemble. L_i is the Hönl-London factor, v is the rovibrational transition frequency, and C is a constant that includes the vibrational transition dipole moment and a collection of other physical constants [45]. The quantity Q_r in the denominator is the rotational partition function and has the form

$$Q_r = \sum_j g_I(2j+1)e^{-\frac{E_j}{k_B T_R}}. \tag{3}$$

Eq. (2) and the expression for $\alpha(v)$ are used in a fitting procedure to determine first the rotational temperature and then the density of the molecular ensemble as a function of r. The temperature is determined by fitting the exponential decay of each rotational transition as a function of the rotational ground state energy (Fig. 4b). To generate the data points in Fig. 4b the absorption values are divided by both the pre-factors in Eq. (2) and the absorption lineshape $g(v)$, leaving only ρs_i. We then take the natural logarithm of the data so the changes in rotational temperature and density can be more easily visualized as linear relationships rather than decaying exponentials. The rotational temperature at each r is obtained from the slope of the linear fits. Once the rotational temperature of the ensemble has been determined, the rotational partition function can be calculated. Using the partition function, the molecular density can be determined from the y-intercept of the fits. The fit results for seven radial positions are shown in Fig. 4c. As expected, the molecular density is largest on the jet axis and decreases steadily with increasing radius. More interesting is the radial dependence of the rotational temperature of the supersonic jet. The coldest rotational temperature observed does not appear at the center of jet. Instead, a temperature of 9 ± 0.9 K is observed on the jet axis, the temperature then drops to 5.5 ± 0.7 K at $r = 4$ mm before rising to 12 ± 1.6 K at the edge of the jet ($r = 10$ mm).

To gain a better understanding of how the jet evolves as it expands from the valve, we have performed height and frequency scans at five distances from the nozzle ($z = 3.5$, 6, 8.5, 11 and 13.5 mm). The procedures described in Figs. 3 and 4 were used to convert the integrated absorption measurements into density and rotational temperature distributions at each measurement distance. The radial distributions calculated for each z-position were then combined into a 2D 'map' describing the rotational temperature and density distributions (z,r) within the measurement volume. To generate a smooth plot of the spatially-varying rotational temperature and density, a 2D spline was used to interpolate between the five radial distribution curves. The resulting 2D density and rotational temperature maps are shown in Fig. 5. The data used to construct this map, acquired at a 2 Hz valve rate and without an automated system for moving the nozzle, was recorded in 28 h.

The density map on the right side of Fig. 5 shows a well-collimated and high molecular density region centered on the jet axis. The collimated packet is surrounded by a lower density cloud of molecules that expands as a function of distance from the nozzle. The most prominent feature of the rotational temperature map is the well-understood cooling of the rotational temperature as a function of distance from the nozzle [47]. However, the temperature map also shows a more subtle effect. The coldest rotational temperatures are not located on the jet axis. Rather, this temperature minimum exists in a ring around the jet axis. Also, the radius of this ring appears to increase with increasing distance form the nozzle. To verify the results of our tomographically reconstructed temperature map, we performed a couple of confirmation checks to make sure that what we observe does not arise from a systematic error in either our absorption measurements or our procedure for tomographic reconstruction. First, we analyzed the P-branch data and found that the tomographic reconstructions for both the density and temperature maps were in good agreement with the maps derived from the R-branch measurements. To rule out systematic error in our tomographic reconstruction procedure, we performed a two-exponential (or two-temperature) fit of the

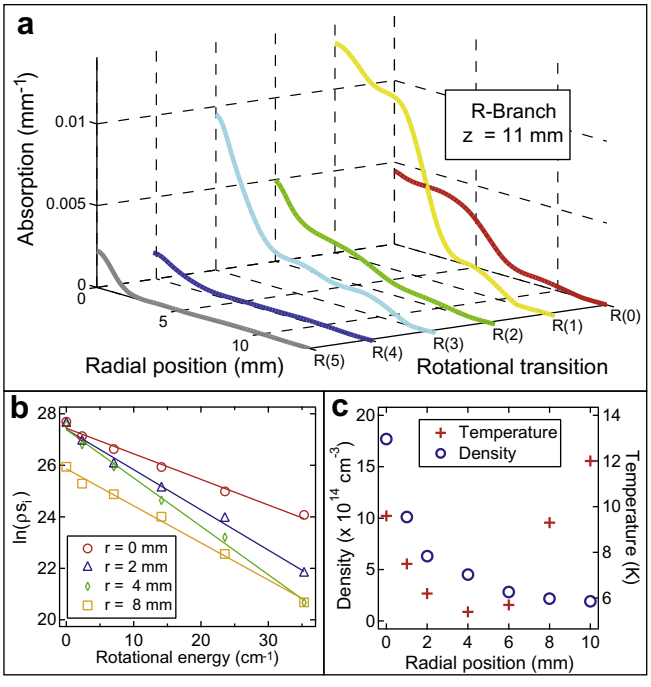

Fig. 4. (a) Tomographically reconstructed radial absorption profiles for the R-branch transitions at a distance of $z = 11$ mm from the nozzle. (b) The density and rotational temperature of the jet are determined by fitting the rotational absorption profile to a Boltzmann distribution at several radii from the beam axis. (c) The radial density and rotational temperature distributions from the fits in (b) show that the C_2H_2 density is largest on the beam axis with a steady decrease toward the edge of the beam. Counterintuitively, the radial temperature distribution reveals a warmer temperature of 9 K at the center of the beam that reduces to 5.5 K at $r = 4$ mm before warming to 12 K near the edge of the jet.

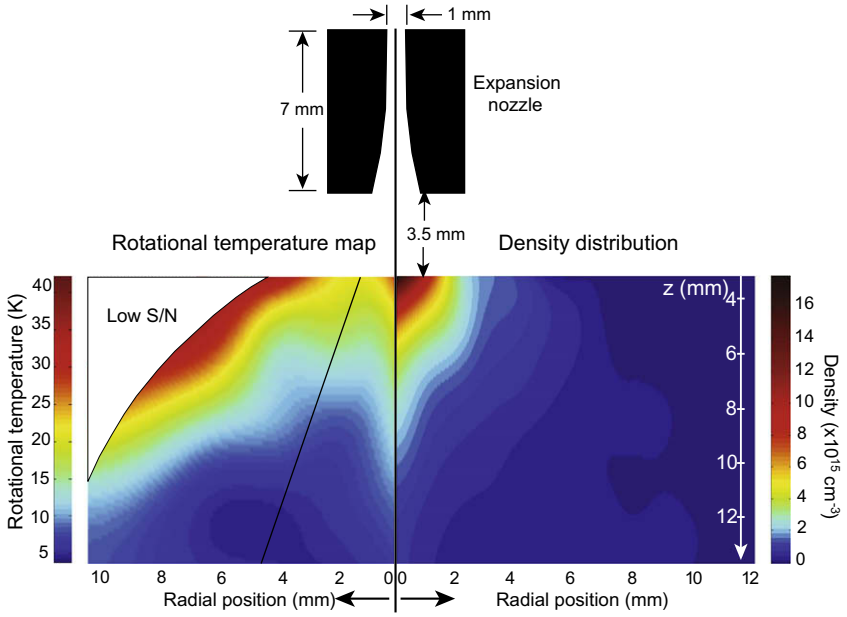

Fig. 5. A scaled drawing of the supersonic expansion nozzle is shown above tomographically reconstructed 2D (z,r) maps of the rotational temperature (left) and density (right). The temperature map reveals the typical rotational cooling as a function of distance from the nozzle. The radial temperature distribution shows that the coldest molecules in the jet reside at a radial position that increases with increasing distance from the nozzle. The diagonal black line on the temperature map defines a molecular trajectory corresponding to molecules with a transverse velocity of 230 m/s. The significance of this trajectory will be discussed in conjunction with the absorption lineshapes shown in Fig. 6. The density distribution shows a well collimated jet centered at $r = 0$ mm surrounded by an expanding cloud of lower density molecules.

rotational distributions for the height-dependent integrated absorption measurements. These fits showed a higher rotational temperature for the $y = 0$ mm measurements, which then decreased as the values of y increased. Finally, the temperature indicated by the fits increased toward the edge of the jet. In short, we confirmed that the temperature map in Fig. 5 faithfully represents the position-dependent rotational temperature of the beam.

To gain some insight into the cause of the observed rotational temperature distribution, we turn our attention to position and rotation dependance of the integrated absorption lineshapes. The absorption lineshapes for the R-branch transitions 0–5 measured at $y = 0$ mm are shown in Fig. 6a for nozzle distances of $z = 3.5$ mm–$z = 16$ mm. To aid in the discussion of the lineshapes in Fig. 6a, we have divided the frequency axis of each graph into three regions (I, II, and III) as denoted in the R(0) graph.

One interesting feature of these lineshapes is shown in Fig. 6b. Here we have plotted the frequency-integrated absorption signals of the R(0) and R(5) transitions as a function of distance from the nozzle. To provide some context for these curves, consider what the frequency-integrated absorption signal would look like for a collisionless expanding jet with a Gaussian velocity distribution. As the jet begins to expand, the signal changes very little until the point where the jet diameter becomes larger than the optical detection beam (cavity mode). Beyond this point, the amplitude of the absorption signal will decrease as a function of distance from the nozzle at the asymptotic rate of z^{-1}. Also, as the amplitude decreases, the lineshape remains constant. In contrast, the signal for R(0) decreases at the much slower rate of $z^{-0.26}$ while the signal for R(5) decreases at the much faster rate of $z^{-2.1}$. The reason for the slow reduction of the R(0) signal and the fast reduction of the R(5) signal is due to rotational cooling of the molecules in the supersonic expansion.

Another interesting feature of the absorption lines are the anomalous shapes that differ considerably from the expected Gaussian lineshape. While anomalous lineshapes have been observed in a continuous beam of C_2H_2/Ar, those anomalies manifest themselves as a dip in the center of the absorption line for the lowest rotations ($j = 0, 1, 2$), and were attributed to C_2H_2 clustering occurring at regions of high density within the beam [25]. In contrast, low rotations in our measurements always exhibit peaks at the line-center. Furthermore, due to the large nozzle aperture and low stagnation pressure in our experiment compared to [25], we suspect that the primary cause of the lineshape anomalies observed here is not due to clustering [48].

The anomalies in our observations tend to occur at frequencies within the lightly shaded region II between 100 MHz and 200 MHz. In this frequency range we observe a depletion of the absorption signal for higher rotation molecules ($j = 2, 3, 4$ and 5) and an excess of signal for the low rotations ($j = 0$ and 1). The data in Fig. 6c shows the absorption trends as a function of nozzle distance for the transitions R(0), R(2) and R(4) for the Doppler shift frequencies of 0 MHz ($v_t = 0$ m/s) and 150 MHz ($v_t = 230$ m/s). Since the nuclear-spin states are not changed by the rotational cooling of the supersonic expansion, the parity of the rotational ground states does not change [49]. Hence, rotational cooling in the expansion proceeds in steps of $\Delta j = 2n$ where n is an integer. The data in Fig. 6c illustrates the transverse velocity dependence of the rotational cooling of molecules with even rotational ground states. At zero transverse velocity, the power law decay exponents of the absorption signals are -0.16, -0.2, and -1.5 for R(0), R(2), and R(4), respectively. While at $v_t = 230$ m/s the decay exponents are -0.14, -1, and -2.4. Comparing the two sets of decay exponents shows that the absorption signals for R(2) and R(4) decay much slower at $v_t = 0$ m/s than at $v_t = 230$ m/s. In contrast, the exponents for R(0) show a comparable decay of the $v_t = 0$ m/s and $v_t = 230$ m/s signals. This can be seen clearly in the ratios of the absorption at $v_t = 230$ m/s versus $v_t = 0$ m/s for each rotation (Fig. 6d). A further analysis of these decay exponents could be used to determine the population transfer rates between the different rotations. However, for the present work we only wish to point out that the population transfer apparently depends on the transverse velocity of the molecules within the jet.

The lineshape measurements and subsequent analysis shown in Fig. 6 can offer some insight into the interesting rotational temper-

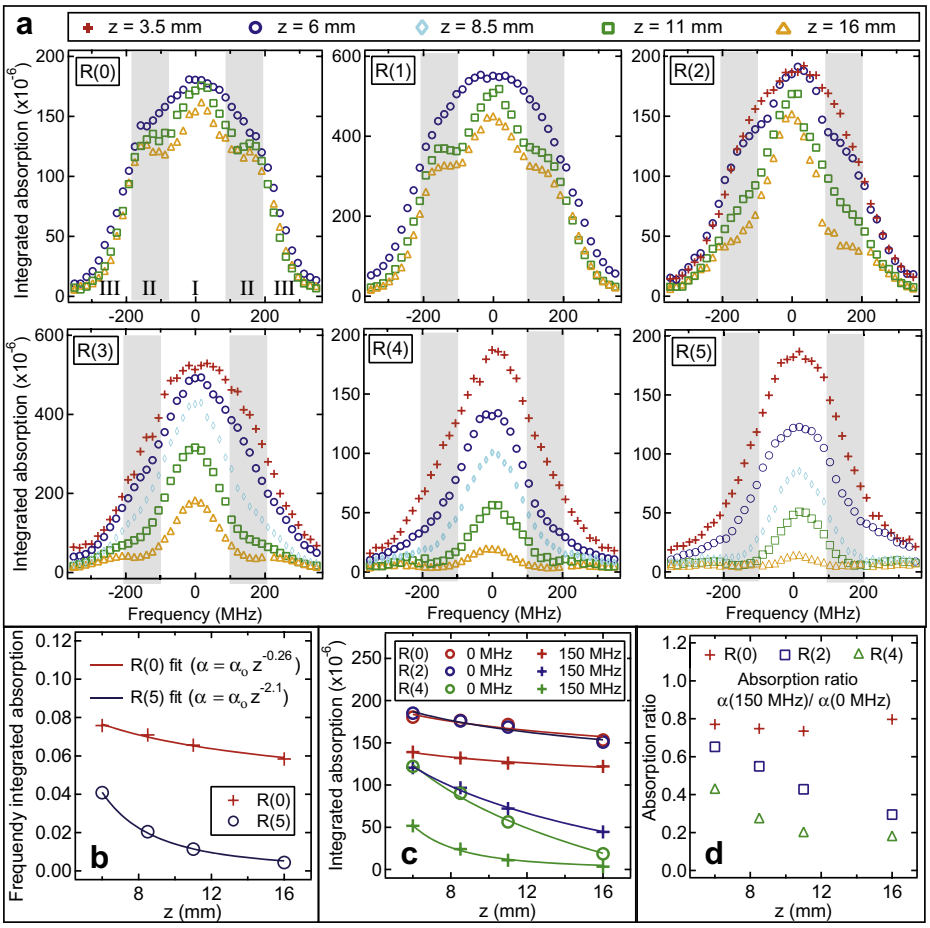

Fig. 6. (a) The absorption lineshapes for R-branch transitions 0–5 measured through the jet axis at $y = 0$ mm for nozzle distances ranging from $z = 3.5$ mm to $z = 16$ mm. Each panel has been labeled with three regions of interest. The light area between the two shaded regions (I) shows the low transverse velocity behavior, the shaded regions (II) show the medium transverse velocity behavior, and the outer light regions (III) show the high transverse velocity behavior. (b) The frequency-integrated absorption signals for R(0) and R(5) versus nozzle distance showing a signal decay that is slower than z^{-1} for R(0) and faster for R(5). (c) Frequency-dependent integrated absorption signals for R(0), R(2), and R(4) at transverse velocities of 230 m/s and at 0 m/s. (d) Absorption ratios of the $v_t = 230$ m/s versus $v_t = 230$ m/s molecules for transitions R(0), R(2), and R(4) show a faster decay of $v_t = 230$ m/s molecules for the higher rotational levels.

ature map of Fig. 5. Once again we consider the center frequency of the darkly shaded 'anomalous' regions in Fig. 6a ($f = 150$ MHz), which has a transverse velocity of 230 m/s. This velocity and the average forward velocity of the jet ($v_f = 650$ m/s), result in a trajectory illustrated by the diagonal black line in the rotational temperature map of Fig. 5. The interesting feature of this trajectory is that it closely follows the minimum rotational temperature as the jet expands. Since the anomalous characteristic of this frequency range is a depletion of higher rotations and an excess of lower rotations, molecules at these velocities will exhibit a lower rotational temperature than other frequency regions. Furthermore, since this same temperature dependence is manifested in the position of the 'rotationally coldest' molecules in Fig. 5, it indicates that the transverse velocities of molecules in the jet are strongly correlated to their position in the jet. Again, further analysis could be implemented to determine the level of correlation between position and velocities of molecules within the jet.

4. Conclusions

The measurements presented in this paper provide a general example of how CE-DFCS systems can be used to rapidly obtain highly detailed information about complex molecular ensembles. In particular, we have demonstrated how CE-DFCS is used to obtain simultaneous high sensitivity, high resolution, and broad-bandwidth spectroscopic measurements. In the present study, the ability to rapidly record broad-bandwidth and high resolution spectra has allowed us to perform tomographic reconstructions of the density and temperature distributions of a C_2H_2/Ar supersonic expansion. These reconstructions reveal an interesting behavior of the position dependance of the rotational temperature distribution. Our ability to observe the absorption lineshapes of each rotational line as a function of distance from the nozzle allows us to interpret the anomalous rotational temperature distribution as resulting from a transverse-velocity dependent rotational cooling rate. Comparing the position and lineshape data also allows us to infer strong correlations between the radial velocity and the radial position of molecules in the supersonic jet.

Acknowledgements

We thank B. Sawyer, K. Lehmann, T. Schibli, and J.L. Hall for useful discussions and AFOSR, DARPA, NIST, and NSF for funding. Corresponding author: M.J. Thorpe (thorpe@jilau1.colorado.edu).

References

[1] M.J. Thorpe, K.D. Moll, R.J. Jones, B. Safdi, J. Ye, Science 311 (2006) 1595.
[2] M.C. Stowe, M.J. Thorpe, A. Pe'er, J. Ye, J.E. Stalnaker, V. Gerginov, S.A. Diddams, Adv. Atom. Mol. Opt. Phys. 55 (2008) 1.

[3] C. Gohle, B. Stein, A. Schliesser, T. Udem, T.W. Hänsch, Phys. Rev. Lett. 99 (2007) 263902.
[4] M.J. Thorpe, J. Ye, Appl. Phys. B 91 (2008) 397.
[5] S.T. Cundiff, J. Ye, J.L. Hall, Rev. Sci. Instrum. 72 (2001) 3749.
[6] T. Udem, R. Holzwarth, T.W. Hänsch, Nature 416 (2002) 233.
[7] A. O'Keefe, D.A.G. Deacon, Rev. Sci. Instrum. 59 (1988) 2544.
[8] J. Ye, L.S. Ma, J.L. Hall, Opt. Lett. 21 (1996) 1000.
[9] Y. He, B. Orr, Appl. Opt. 44 (2005) 6752.
[10] E.R. Crosson, P. Haar, G.A. Marcus, H.A. Schwettman, B.A. Paldus, T.G. Spence, R.N. Zare, Rev. Sci. Instrum. 70 (1999) 4.
[11] M.D. Levenson, B.A. Paldus, T.G. Spence, C.C. Harb, J. Harris, J.S.R.N. Zare, Chem. Phys. Lett. 290 (1998) 335.
[12] D. Romanini, K.K. Lehmann, J. Chem. Phys. 99 (1993) 6287.
[13] M.J. Thorpe, D. Balslev-Clausen, M.S. Kirchner, J. Ye, Opt. Express 16 (2008) 2387.
[14] K.-K. Ni et al., Science 322 (2008) 231.
[15] J. Doyle, B. Friedrich, K.R.V.F. Masnou-Seeuws, Eur. J. Phys. D 31 (2004) 149.
[16] A. André et al., Nature Phys. 2 (2006) 636.
[17] B.C. Sawyer, B.L. Lev, E.R. Hudson, B.K. Stuhl, M. Lara, J.L. Bohn, J. Ye, Phys. Rev. Lett. 98 (2007) 253002.
[18] S.Y.T. Van De Meerakker, H.L. Bethlem, G. Meijer, Nature Phys. 4 (2008) 595.
[19] J.G. Danzl et al., Science 321 (2008) 1062.
[20] M. Viteau, A. Chotia, M. Allegrini, N. Bouloufa, O. Dulieu, D. Comparat, P. Pillet, Science 321 (2008) 232.
[21] W. Salzmann et al., Phys. Rev. Lett. 100 (2008) 233003.
[22] A. Pe'er, E.A. Shapiro, M.C. Stowe, M. Shapiro, J. Ye, Phys. Rev. Lett. 98 (2007) 113004.
[23] E.A. Shapiro, A. Pe'er, J. Ye, M. Shapiro, Phys. Rev. Lett. 101 (2008) 023601.
[24] G. Tejeda, B. Maté, J.M. Fernández-Sánchez, S. Montero, Phys. Rev. Lett. 76 (1996) 34.
[25] K. Didriche, C. Lauzin, P. Macko, W.J. Lafferty, R.J. Saykally, M. Herman, Chem. Phys. Lett. 463 (2007) 345.
[26] M. Herman, K. Didriche, D. Hurtmans, B. Kizil, P. Macko, A. Rizopoulos, P. Van Poucke, Mol. Phys. 105 (2007) 815.
[27] J.J. Scherer, J.B. Paul, A. O'Keefe, R.J. Saykally, Chem. Rev. 97 (1997) 25.
[28] R.N. Brancewell, Fourier Transform and it's Applications, third edn., McGraw-Hill, 2000.
[29] F. Tauser, A. Leitenstorfer, W. Zinth, Opt. Express 11 (2003) 594.
[30] J. Ye, S.T. Cundiff, Femtosecond Optical Frequency Comb Technology: Principle Operation and Application, Springer, New York, 2005.
[31] D.J. Jones, S.A. Diddams, J.K. Ranka, A. Stentz, R.S. Windeler, J.L. Hall, S.T. Cundiff, Science 288 (2000) 635.
[32] T. Gherman, D. Romanini, Opt. Express 10 (2002) 1033.
[33] R.J. Jones, J.C. Diels, Phys. Rev. Lett. 86 (2001) 3288.
[34] R. Bakowski, L. Corner, G. Hancock, R. Kotchie, R. Peverall, G.A.D. Ritchie, Appl. Phys. B 75 (2002) 745.
[35] S.A. Diddams, L. Hollberg, V. Mbele, Nature 445 (2007) 627.
[36] A. Vega, A.M. Weiner, C. Lin, Appl. Opt. 42 (2003) 4152.
[37] S. Xiao, A.M. Weiner, Opt. Express 12 (2004) 2895.
[38] S. Xiao, A.M. Weiner, C. Lin, IEEE J. Quantum Electron. 40 (2004) 420.
[39] A.A. Madej, A.L. Alcock, A. Czajkowski, J.E. Bernard, S. Chepurov, J. Opt. Soc. Am. B 23 (2006) 2200.
[40] L.S. Rothman et al., J. Quant. Spectrosc. Radiat. Transfer 96 (2005) 139.
[41] J.L. Hall, M.S. Taubman, J. Ye, Laser Stabilization, OSA Handbook, p. 14.
[42] U. Valbusa, Atomic and Molecular Beam Methods 1 (1988) 443.
[43] S.R. Deans, The Radon Transform and Some of its Applications, Wiley, New York, 1983.
[44] E.W. Hansen, A. Jablokow, IEEE. Trans. Acous. Speech Sig. Proc. 30 (1982) 874.
[45] G. Herzberg, Molecular Spectra and Molecular Structure, second edn., vol. I, Krieger, 1950.
[46] G. Herzberg, Molecular Spectra and Molecular Structure, vol. II, Krieger, 1945.
[47] D.R. Miller, Atomic and Molecular Beam Methods 1 (1988) 14.
[48] W.R. Gentry, Atomic and Molecular Beam Methods 1 (1988) 70.
[49] M.D. Duncan, P. Osterlin, R.L. Byer, Opt. Lett. 6 (1981) 90.